Wide-field, surface-sensitive four-wave mixing microscopy of nanostructures

Yong Wang, Xuejun Liu, Aaron R. Halpern, Kyunghee Cho, Robert M. Corn, and Eric O. Potma*

Department of Chemistry, University of California, Irvine, Irvine, California, 92697-2025, USA

*Corresponding author: epotma@uci.edu

Received 13 February 2012; accepted 14 March 2012;
posted 2 April 2012 (Doc. ID 162962); published 24 May 2012

We describe a wide-field four-wave mixing (FWM) microscope with imaging characteristics optimized for examining nanostructures. The microscope employs surface-plasmon polariton (SPP) excitation in a gold film to achieve surface-sensitive imaging conditions. The SPP surface fields boost the FWM efficiency by 2 orders of magnitude relative to the excitation efficiency of the evanescent fields at a bare glass surface. We demonstrate two excitation geometries that completely suppress the electronic FWM response of the metal film while allowing the far-field detection of FWM radiation from nanostructures at the interface. We obtained wide-field FWM images from individual carbon nanotubes and nanoclusters of neocyanine molecules at image acquisition times of 1 s, demonstrating the potential for background free, surface-enhanced FWM imaging of nanomaterials.

OCIS codes: 190.4223, 240.6680.

1. Introduction

Four-wave mixing (FWM) techniques comprise a class of nonlinear optical methods sensitive to both the electronic and vibrational properties of materials. When combined with microscopic focusing, the FWM response forms a useful probe for investigating the nonlinear optical properties of individual microstructures and nanostructures, including single molecular compounds [1]. For instance, the vibrational sensitivity of FWM techniques has been used extensively to acquire high-resolution chemical maps of biological samples [2,3], whereas the electronic FWM sensitivity has been used to study the nonlinear optical response of single metallic and semiconducting nano structures [4–6].

It has proven difficult, however, to extend the versatility of FWM techniques to the research area of molecules and structures at surfaces. FWM probes the third-order nonlinear susceptibility ($\chi^{(3)}$) of the material. Under phase-matched conditions, $\chi^{(3)}$ processes are generally bulk allowed. Unlike nonlinear optical techniques that are sensitive to the second-order susceptibility ($\chi^{(2)}$), such as sum-frequency generation spectroscopy (SFG) and second harmonic generation (SHG) [7,8], $\chi^{(3)}$-based techniques do not exhibit an intrinsic surface sensitivity. Consequently, contributions from bulk media and supporting substrates can overshadow the FWM signal from surface-bound structures. These experimental limitations have complicated the application of FWM techniques to surface-specific spectroscopy and chemical sensing, especially in the area of microscopy.

One approach to enhance the FWM sensitivity to surface-bound structures is to exploit the excitation of strong evanescent fields at substrate surfaces. In particular, the surface fields associated with surface-plasmon excitations at metal surfaces have been successfully used to enhance optical effects at interfaces [9]. Examples include surface-enhanced Raman scattering [10–12] and fluorescence [13–15], which are enabled by the strongly localized electric fields that are confined to the surface of metallic nanostructures. In addition, the feasibility of using localized surface-plasmon modes for enhancing FWM signals

1559-128X/12/163305-08$15.00/0

of molecules near surfaces has been demonstrated in coherent anti-Stokes Raman scattering (CARS) studies [16–20] and in stimulated Raman scattering (SRS) experiments [21].

While structures that support localized surface plasmons are useful for boosting FWM signals, they are currently less suitable for performing quantitatively meaningful measurements, due to the often ill-defined geometries and surface chemistry of the nanometallic substrates. In this regard, the use of surface-plasmon modes at flat metallic thin films, which have precisely controlled surface properties, offer an attractive strategy for the near-field characterization of surface-bound structures. The generation of FWM at metallic thin films has recently attracted considerable attention. Because FWM uses multiple incident beams, the spatial phase of the nonlinear surface polarization can be manipulated by adjusting the excitation configuration, producing interesting optical effects at the metal interface. For instance, freely propagating excitation fields can selectively excite surface-bound FWM fields [22–24]. In addition, the excitation geometry can be chosen such that the nonlinear surface polarization radiates in an anomalous far-field direction, corresponding to an effective negative refractive index of the Au thin film [25].

However, the strong FWM response from the metal film complicates the detection of nonlinear signals from nonmetallic, surface-bound objects, which can be significantly weaker. In order to exploit the versatility of FWM for surface-sensitive measurements of structures near thin metal films, excitation geometries need to be developed that optimize the signal from surface-bound compounds while suppressing the FWM response of the metal substrate itself. As early as 1979, it was shown that the controlled excitation of surface-plasmon polaritons (SPPs) in a gold film enables the registration of CARS signals from molecular liquids near the metal surface [26]. A related SPP-based scheme was recently implemented for microscopic imaging of nanostructures [27]. In the latter scheme, the intrinsic FWM of the metal film was suppressed by using a counterpropagating excitation configuration with focused laser beams, enabling efficient probing of surface-enhanced $\chi^{(3)}$ signals from individual nanoparticles.

While previous work has shown that SPP-mediated $\chi^{(3)}$ signals can be generated from (nonmetallic) objects near the metal surface, existing implementations are not suitable for generating actual images. In the current work, we describe an imaging implementation of surface-sensitive FWM microscopy that enables probing of the nonlinear properties of nanostructures on surfaces. Unlike previous microscopy implementations, we use a new illumination scheme that is not based on focused beams but instead uses full wide-field illumination and detection. Analogous to total internal reflection fluorescence (TIRF) microscopy [28], this wide-field FWM approach enables direct inspection of structures near the surface within a large field of view. We will discuss specific phase-matching configurations that suppress the FWM contributions from the substrate and that optimize the surface-enhanced nonlinear signals from nanoscopic objects.

2. Materials and Methods

A. Microscope Setup

In the experiments described in this work, we have used a dual-color CARS-like FWM scheme in which two incident fields (ω_1, ω_2) induce a nonlinear polarization at frequency $\omega_3 = 2\omega_1 - \omega_2$. The ω_1 beam was derived from an optical parametric oscillator (OPO, Inspire, Spectra-Physics), synchronously pumped by a 80 MHz, femtosecond Ti:sapphire laser (MaiTai, Spectra-Physics). The 230 fs signal pulses from the OPO were set to 728 nm. The 200 fs pulse train of the fundamental was fixed at 820 nm, and was used as the ω_2 beam in the experiments. Using these beam parameters, the FWM signal is generated at 650 nm.

The excitation beams were directed to a wide-field microscope, which consists of a high numerical objective (40×, NA 0.6), a tube lens, a 650 nm (±20 nm) bandpass filter, and an imaging CCD camera (Clara, Andor). The general layout is sketched in Fig. 1A. Two different excitation geometries were implemented. In both geometries, the incident beams illuminate the sample through a BK7 prism. The sample consists of a borosilicate glass slide (Schott), coated with a 44 nm gold film. The glass side of the coverslip is interfaced with the prism using immersion oil, while the gold surface is exposed to the air. The first geometry, sketched in Fig. 1B, is a collinear excitation scheme. Both the ω_1 and ω_2 beams were shallowly focused with a lens such that beam diameter was ~150 μm at the sample plane. The angle of each beam is tuned to the respective Kretschmann angle for efficient SPP excitation (43.1° for ω_1; 42.6° for ω_2). In this scheme, SPPs at the ω_1 and ω_2 frequencies are launched in a collinear fashion. In the second geometry, given in Fig. 1C, the ω_1 and ω_2 beams enter the prism from opposite sides, producing counterpropagating SPP modes. The average power at the sample, integrated over the full illumination area, was 100 mW for the ω_1 beam and 150 mW for the ω_2 beam. The image integration time was between 0.1 s and 3 s, depending on the strength of the FWM signal.

B. Sample Preparation

Gold thin films were evaporated to a thickness of 44 nm on borosilicate glass slides, which were pretreated with a 1 nm Cr adhesion layer. For patterned Au films, lithographic masks were used to deposit S1827 photoresist (MicroChem) onto the surface, followed by chemical etching. Patterns consisting of 10 μm wide Au stripes, with a spacing of 10 μm between the stripes, were fabricated for the experiments. The gold-covered slides were cleaned in an oxygen plasma. Several μL of a suspension of

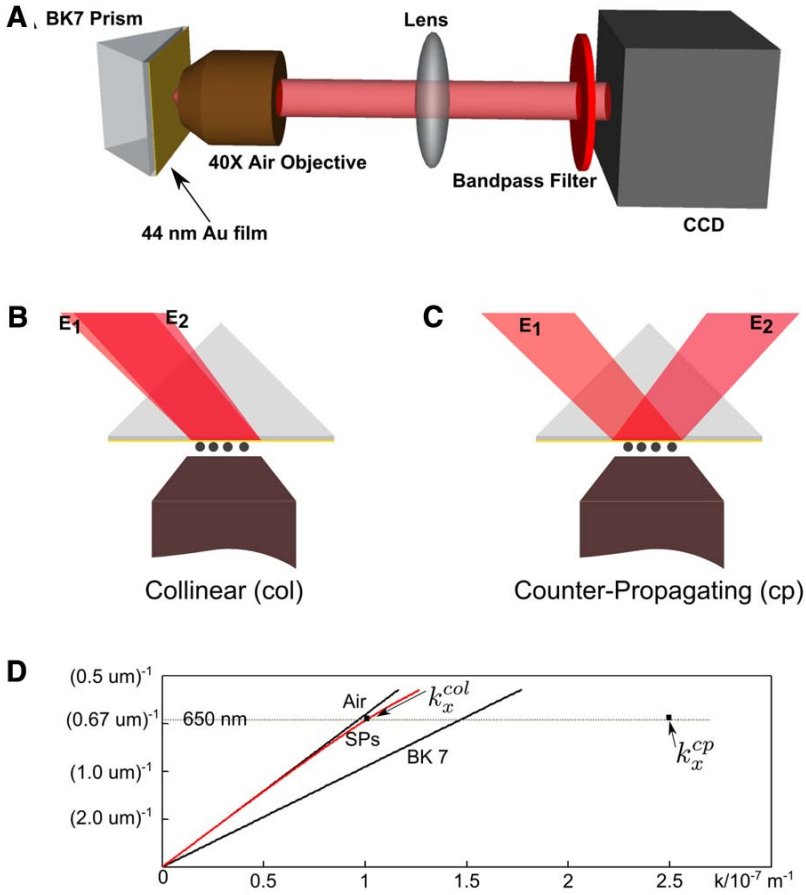

Fig. 1. (Color online) Schematic of the experimental setup. A, the glass slide holding the sample is mounted on a BK7 prism and FWM radiation is collected on the air side of the Au film using a high numerical aperture lens. A tube lens is used to form an image onto a CCD camera. FWM radiation is filtered with a bandpass filter. B, collinear excitation geometry. Nanoparticles deposited on the Au film are symbolized by the black dots. C, counterpropagating excitation geometry. D, dispersion of the lateral component of the SPP wave vector. Red line indicates the dispersion of the SPP wave vector at the Au/air interface. Solid black lines give the wave vector of freely propagating light in air and in glass (BK7). The SPP wave vectors at the FWM frequency (ω_3, 650 nm) are indicated for both the collinear and counterpropagating geometries.

30 nm silicon nanoparticles (Melorium) in methanol was applied to the surface and allowed to dry.

Multiwalled carbon nanotubes suspended in water were purchased from Nanostructured and Amorphous Materials, Inc. The suspension was dried to a black powder. The dry material was suspended in dichloromethane and sonicated for 30 minutes. The suspension was kept overnight to let precipitates accumulate at the bottom of the flask. Several μL of the clear solution was pipetted out of the flask and suspended on the gold-covered slides. After evaporation of the solvent, the slides were used for the imaging studies. Scanning electron microscopy (SEM) images were taken with a FEI Quanta 3D FEG Electron Microscope, using a voltage of 1.00 kV and a current of 5.33 pA.

Neocyanine was purchased from ACROS Organics and used without further purification. Using a syringe, 100 μL of a 0.25 mM neocyanine solution in methanol was applied to a borosilicate microscope slide. After evaporation of the solvent, a distribution of microsized and nanosized neocyanine clusters was obtained on the glass surface. The surface was subsequently brought into contact with a patterned polymethylsiloxane (PDMS) layer. The PDMS layer featured 10 μm wide stripes with an interstripe distance of 10 μm, fabricated by molding the layer on a S1827 photoresist grating. Upon lifting the patterned PDMS layer from the neocyanine covered glass surface, a fraction of the neocyanine clusters was removed from the glass. The PDMS layer was subsequently brought into contact with a gold coated glass coverslip. Gentle contact between the PDMS layer and the gold film resulted in the deposition of neocyanine clusters on the gold surface.

3. Experimental Results

A. Surface-Plasmon Enhanced FWM

To increase the sensitivity of the wide-field FWM microscope to nanostructures, the excitation geometries in this study were chosen such as to minimize the intrinsic FWM signal of the Au film. The FWM radiation is detected on the air side of the metallic film. In Fig. 1D, the dispersion of the lateral component of the wave vector (k_x) at the gold–air interface is

shown. For the collinear geometry, the wave vector k_x^{col} of the SPP mode at the FWM radiation frequency (ω_3, 650 nm) is larger than the wave vector for the freely propagating radiation. This implies that no FWM emission from the film is expected in the far field when the detector is configured on the air side of the Au interface. Note that if the detector is placed on the glass side of the interface, leakage radiation into the far-field is allowed and FWM radiation can be expected for the collinear excitation geometry. In the counterpropagating geometry, the far-field FWM radiation from the film is forbidden in all far-field propagation directions. In Fig. 1D, the counterpropagating wave vector k_x^{cp} at the FWM frequency is much larger than freely propagating light in all directions, resulting in a complete suppression of ω_3 radiation from the induced nonlinear polarization in the film. For both geometries, the $1/e$ depth of the effective evanescent field ($E_1^2 E_2^*$) at the surface is 174 nm, which translates into efficient FWM excitation ($\propto I_1^2 I_2$) over a characteristic length scale of 87 nm within the vicinity of the gold surface.

Although the nonlinear radiation from the film is suppressed, emission resulting from the nonlinear polarization of structures much smaller than the wavelength of light is allowed in the far field. If the amplitude and phase of the nonlinear polarization in such nanostructures is different from the polarization in the film, then the structures act as dipole-like radiators whose radiation is allowed in the far field [29]. In Fig. 2A, the far-field FWM image of a collection of Si nanoparticles is shown for the collinear SPP excitation geometry. A white light transmission image is superimposed to highlight the striped pattern of the gold film. It can be seen that, whereas the Au film produces no FWM radiation, the FWM signal from individual Si particles is readily detected. We note that the variation in the signal intensity is most likely due to tentative clustering of the nanoparticles at some of the locations.

In Fig. 2B, the same FWM image is shown without the transmission image superimposed. The FWM signal is only observed from the Si particles that are located on the Au film. The particles located on the bare glass surface produce FWM signals that are at least 10^2 times weaker than the FWM signals observed from particles on the gold film. This figure indicates that the surface fields at the metal/air interface are significantly stronger than the (evanescent) fields at the glass/air interface. In other words, the FWM signal from the Si particles on the Au film is surface-*enhanced* by the SPP excitation in the film.

Figure 2C highlights that the observed FWM signal results from a process that depends on the presence of surface fields at both ω_1 and ω_2. When the temporal delay between the beams is offset, the FWM signal disappears accordingly. Similarly, if the excitation polarization orientation of the incident beams is changed from P to S, no FWM signal can be seen. The signal also disappears when the input angle of either of the incident beams is different from the Kretschmann angle. These latter results confirm that the surface excitation fields of the SPP mode are responsible for the enhanced FWM radiation of the nanostructures at the surface. These experiments show that wide-field, surface-enhanced FWM signals from nanostructures can be obtained that are free from FWM background radiation from the substrate.

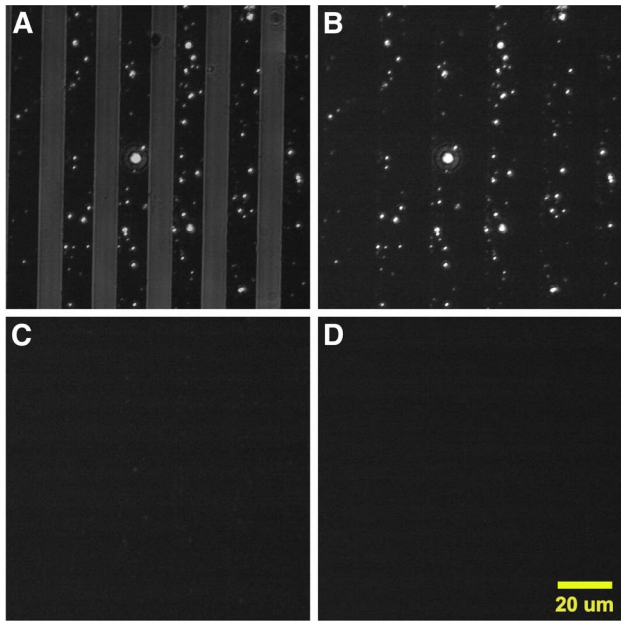

Fig. 2. (Color online) Surface-enhanced FWM of Si nanoparticles. A, far-field FWM image of Si nanoparticles on a 10 μm-striped Au film. The transmission image obtained by illuminating the sample with white light is shown in gray. B, same image as in A without the transmission image. C, FWM image when the excitation beams are temporally offset (−500 fs). D, FWM image when the incident beams are S polarized with respect to the Au film.

In addition to the FWM signals from the particles, FWM contributions that are initially generated in the film and subsequently scattered at the particle, i.e., $\chi^{(1)}$-related scattering, can add to the signal observed. We found this contribution to be negligible. When the silicon particles are replaced with materials characterized by a lower $\chi^{(3)}$, the FWM signal decreases correspondingly. For instance, the FWM signals from 150 nm silica particles, which are at the noise floor of the CCD camera, are at least 3 orders of magnitude weaker than the FWM signals from smaller-sized silicon nanoparticles. Given that the $\chi^{(3)}$ of silica is 4 orders of magnitude smaller than the $\chi^{(3)}$ of silicon [1], a much lower FWM response of silica is expected based on the difference in $\chi^{(3)}$ alone. This observation thus provides evidence that the signals detected are dominated by the $\chi^{(3)}$ response of nanoparticles, and that the contribution stemming from the linear scattering of surface fields at nanoscopic objects is negligible.

B. Collinear and Counterpropagating Excitation Geometries

In the collinear excitation geometry, leakage radiation at ω_3 in the direction of the glass substrate is allowed. This may tentatively produce back-reflected

stray light that can interfere with the direct dipole-like emission from the nanostructures at the far-field detector. This problem is absent in the counterpropagating scheme, which fully suppresses FWM radiation from the film.

The two excitation geometries have, however, different imaging properties beyond their background suppression capabilities. In Figs. 3A–3E, wide-field FWM images from Si nanoparticles on a uniform Au film are shown as a function of the time delay between the incident fs beams. Upon changing the time delay between the beams away from zero time delay, the FWM signal decreases as expected. The insets show the calculated excitation efficiency within the field of view for each of the time delays. Longer time delays result in a lower excitation density and thus in a reduced FWM signal. In the counterpropagating excitation scheme, the spatial extent of the excitation density is significantly reduced. For each time delay, the overlap zone of the counterpropagating pulses is ~40 μm, which corresponds to the spatial extent of the femtosecond pulses. Upon changing the time delay, the location of the overlap zone shifts within the field of view. The insets show the calculated excitation densities based on the temporal profile of the pulses and their propagation in the Au film. The reduced field of view makes the counterpropagating geometry a less attractive choice for wide-field FWM imaging applications based on fs excitation pulses.

C. Surface-Sensitive FWM of Molecular Nanostructures

The enhanced surface fields in combination with nanostructure specific phase-matching conditions make this wide-field FWM approach a very sensitive method for nonlinear measurements of nanostructures associated with the gold surface. The technique is sensitive enough to detect the FWM response of individual multiwalled carbon nanotubes. In Fig. 4, a wide-field image of a carbon nanotube is shown. FWM radiation from different parts of the nanotube is observed. The signal results from the electronic $\chi^{(3)}$ of the nanotube, as previously shown in FWM imaging studies based on a laser scanning approach [5]. The results presented here show that the FWM response from individual nanotubes can also be detected in a wide-field geometry where, unlike the laser scanning mode, the excitation field is strictly confined to the surface.

In Fig. 5A a wide-field FWM image of microsized and nanosized clusters of the dye neocyanine is shown. Similar to carbon nanotubes, the excitation energies coincide with electronic transitions in the molecule, as shown in Fig. 5B, producing an electronic $\chi^{(3)}$ response at the FWM detection wavelength. This example demonstrates that $\chi^{(3)}$ imaging measurements, sensitive to the electronic properties of molecules, can be performed on compounds excited by fields confined to the gold surface.

4. Discussion

The use of evanescent fields for optical excitation of compounds near the surface of a substrate is a proven strategy in wide-field microscopy. For fluorescence experiments, the evanescent field near a glass surface is sufficient for efficient excitation of chromophores. This principle is exploited in TIRF, which can detect fluorescent compounds down to the single molecule limit [30]. It has been shown that even stronger surface fields can be attained when using SPP excitation in gold films, producing fluorescence signals that are 1 order of magnitude higher compared to regular TIRF [31]. The use of SPP enhanced fields represents a good strategy for generating nonlinear signals near the surface, which typically rely on much higher excitation densities compared to linear fluorescence methods. The SPP enhanced approach has proven successful in a two-photon excited fluorescence

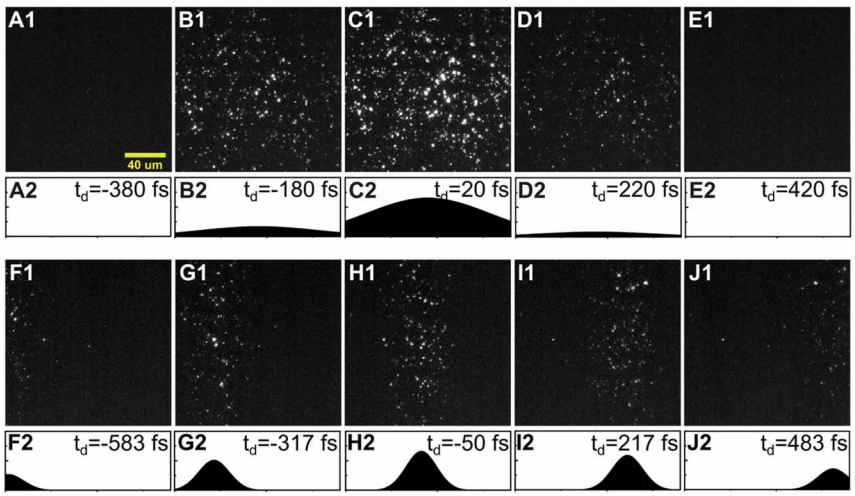

Fig. 3. (Color online) Differences between collinear and counterpropagating excitation schemes. A–E, FWM images in the collinear excitation geometry as a function of time delay between the excitation pulses. F–J, FWM images in the counterpropagating excitation geometry as a function of time delay between the excitation pulses. The insets show the calculated spatio-temporal excitation density ($I_1^2 I_2$) for each time delay.

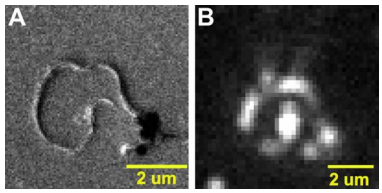

Fig. 4. (Color online) Wide-field FWM imaging of carbon nanotubes using the collinear geometry. A, SEM image of a multiwalled carbon nanotube. B, Corresponding FWM image.

(TPEF) implementation of TIRF [32]. It has also been shown that the SPP modes supported by thin metal films enable surface-enhanced SHG from metallic structures on the film [33,34].

In this work, we have extended these ideas to wide-field FWM imaging. Although the principle of SPP-enhancement of FWM signals has been pointed out, this concept has not been exploited before for the purpose of imaging, i.e., the visualization of distributions of compounds on the surface. Compared to TPEF and SHG, dual-color FWM is more challenging because multiple excitation beams need to be coupled into the metallic film. In addition, in dual-color FWM, a strong $\chi^{(3)}$ contribution of the surface introduces a background that can overwhelm and interfere with the response from individual structures at the surface. We have adopted two geometries that aim to suppress the radiation from the film itself. Both geometries include a far-field detection scheme where the detector is placed on the air side of the gold surface. In this detection direction, direct emission from the gold film is prohibited, while dipole-like radiation of nanoscopic objects is allowed. We found that both collinear and counterpropagating excitation schemes exhibited excellent suppression of FWM contributions from the film. No background contributions were detected above the noise level of the measurements. Although in the counterpropagating scheme the FWM radiation from the film is prohibited in all directions, this additional restriction did not necessarily improve the imaging properties of the wide-field FWM microscope. The collinear excitation geometry is characterized by a larger field of view, because the active imaging area in the counterpropagating scheme is reduced by the smaller overlap area of the excitation pulses.

The wide-field FWM illumination scheme introduced here is different from previous wide-field FWM microscopes that have been used for CARS imaging [35–37]. In particular, the nonlinear signal in SPP-mediated FWM microscopy is intrinsically confined to a region within 100 nm from the metal surface. In addition, the surface field mediated enhancement in FWM efficiency by a factor of 10^2 enables visualization of single nanostructures such as carbon nanotubes without the use of amplified laser systems. Instead, with the field-enhancement in place, the benign pulse energies of high-repetition rate laser oscillators are sufficient for rapid imaging of nanoscopic objects. Hence, the scheme described in this work can be readily applied to conventional coherent Raman scattering and multimodal imaging microscopes.

It is interesting to compare the surface sensitivity of SPP-mediated excitation used here with the sensitivity attained in epidetection of FWM radiation, which is commonly employed in laser scanning microscopy. In laser scanning CARS microscopy, for instance, the epidetected signal is phase-mismatched, which retains signals originating from particles smaller than the wavelength of light but rejects contributions from the bulk [38]. It has been

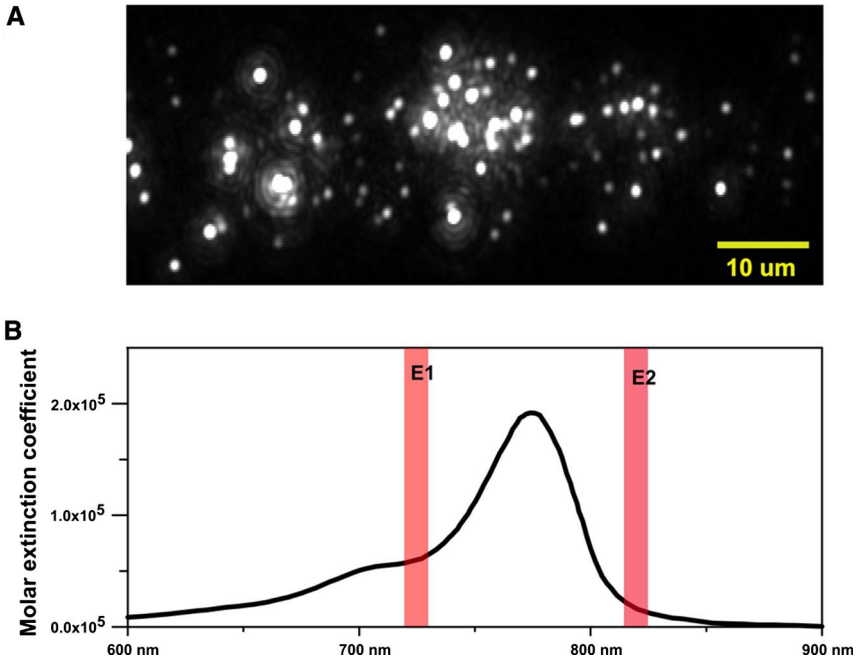

Fig. 5. (Color online) A, Wide-field FWM image of neocyanine microsized and nanosized clusters using the collinear geometry. B, Absorption profile or neocyanine. The shaded areas indicate the excitation wavelengths of the incident beams.

shown that this mechanism increases the CARS sensitivity at interfaces [39]. Nonetheless, conventional epidetection does not suppress the back-reflected nonresonant FWM contributions from the substrate, which can overwhelm the FWM signal from target compounds at the surface. By making use of the unique phase properties of the surface fields at the gold/air interface, the wide-field FWM technique introduced here intrinsically suppresses the far-field FWM radiation from the substrate, and only detects the nonlinear signals from dipole-like radiators. The method discussed rejects background contributions based on lateral object-size, and is thus optimized for sensitive investigations of nanostructures. Note, however, that this wide-field excitation approach is not suitable for detecting FWM radiation from layers of molecules tethered to the surface, as radiation from areas larger than the optical wavelength are phase-mismatched in the far field. Other wide-field excitation schemes, based on detection on the glass side of the substrate, can be employed for imaging samples beyond nanostructures, including molecular layers and biological samples.

In the experiments described in this work, we have taken advantage of the facilitated imaging conditions when the nanostructured material is exposed to air. For more advanced applications, the design needs to be optimized for materials suspended in aqueous environments. Using an objective-based illumination scheme with counterpropagating beams, we expect that surface-sensitive FWM imaging properties similar to the ones described herein can be obtained for samples in aqueous media.

We found experimentally that the use of SPP excitation raised the FWM generation efficiency by at least 2 orders of magnitude. Determination of the exact enhancement factor is somewhat complicated by the inherent size variation among the particles, which produces a variation in FWM intensity within the population and prevents a direct comparison of the response of a single particle on the gold film with the response of a single particle on the bare glass surface. Nonetheless, we find that on the level of the ensemble, the FWM signal from the particle population on the gold film is more than 10^2 times stronger compared to the signal of the population on the glass surface in all of the cases examined.

Despite the substantial improvement of FWM generation efficiency at metallic interfaces, even higher efficiencies will be required to visualize structures with lower $\chi^{(3)}$ properties, such as biological materials and single molecular compounds. In this regard, the use of engineered metallic surfaces for enhancing the FWM excitation efficiency has recently been pointed out. For instance, depositing a thin dielectric layer on the metal surface has been shown to increase the efficiency of FWM generation at surfaces by 4 orders of magnitude [40]. In addition, we note that the image acquisition time and detection noise can be substantially improved when using an electron multiplying CCD (EM-CCD) camera. We have performed preliminary wide-field FWM imaging experiments with EM-CCD cameras and found that the detection sensitivity can be improved by at least an order of magnitude. Such improvements underline the enormous potential of SPP-based FWM imaging, and may bring applications in the area of single molecular imaging within reach.

5. Conclusion

We developed a wide-field FWM microscope for the purpose of nonlinear investigation of nanostructures. This microscope employs SPP excitation of gold films to overcome the bulk properties of the $\chi^{(3)}$ response by suppressing the excitation probability beyond a distance of ~100 nm from the gold surface. The wide-field implementation of SPP enhanced FWM microscopy offers several new features: (i) The wide-field illumination and detection scheme allows direct *imaging* of distributions of nanoparticles on the surface. (ii) The FWM background from the gold surface is eliminated by detecting at the air side of the gold film, a direction in which the far-field radiation from the Au surface is prohibited. (iii) In this configuration we observe only $\chi^{(3)}$-induced signals from nanosized objects at the surface. Such objects exhibit dipole-like radiation and are thus allowed to radiate in the far field. (iv) The evanescent field at the metal surface enhances the FWM efficiency with a factor of 10^2 relative to the evanescent field associated with the glass, ensuring highly efficient and sustained FWM generation from nanoscopic objects. We obtained surface-sensitive, wide-field FWM images of silicon nanoparticles, carbon nanotubes, and clusters of dye molecules, with image acquisition times comparable to what can be achieved with conventional laser scanning FWM microscopy. We expect that with subsequent improvements in detector sensitivity and substrate preparation, the SPP-based wide-field FWM microscope can be a helpful tool in a wide range of imaging applications, including the interrogation of single molecular systems.

We thank Steven Yampolski for his help in earlier editions of the experiments. This work was supported by the Department of Energy, grant DE-SC0003905. We are also thankful to the Center of Chemical Innovation, National Science Foundation, grant CHE-0802913, for providing access to instrumentation. RMC acknowledges funding from the National Science Foundation, grant CHE-0551935.

References

1. Y. Wang, C.-Y. Lin, A. Nikolaenko, V. Raghunathan, and E. O. Potma, "Four-wave mixing microscopy of nanostructures," Adv. Opt. Photon. **3**, 1–52 (2011).
2. C. L. Evans and X. S. Xie, "Coherent anti-Stokes Raman scattering microscopy: chemical imaging for biology and medicine," Annu. Rev. Anal. Chem. **1**, 883–909 (2008).
3. C. W. Freudiger, W. Min, B. G. Saar, S. Lu, G. R. Holtom, C. He, J. C. Tsai, J. X. Kang, and X. S. Xie, "Label-free biomedical imaging with high sensitivity by stimulated Raman scattering microscopy," Science **322**, 1857–1861 (2008).

4. M. Danckwerts and L. Novotny, "Optical frequency mixing at coupled gold nanoparticles," Phys. Rev. Lett. **98**, 026104 (2007).
5. H. Kim, T. Sheps, P. G. Collins, and E. O. Potma, "Nonlinear optical imaging of individual carbon nanotubes with four-wave-mixing microscopy," Nano Lett. **9**, 2991–2995 (2009).
6. Y. Jung, L. Tong, A. Tanaudommongkon, J. X. Cheng, and C. Yang, "In vitro and in vivo nonlinear optical imaging of silicon nanowires," Nano Lett. **9**, 2440–2444 (2009).
7. Y. R. Shen, "Surface properties probed by second-harmonic and sum-frequency generation," Nature **337**, 519–525 (1989).
8. R. M. Corn and D. A. Higgens, "Optical second harmonic generation as a probe of surface chemistry," Chem. Rev. **94**, 107–125 (1994).
9. S. A. Maier, ed., *Plasmonics: Fundamentals and Applications* (Springer, 2007).
10. M. Fleischmann, P. J. Hendra, and A. J. McQuillan, "Raman spectra of pyridine adsorbed at a silver electrode," Chem. Phys. Lett. **26**, 163–166 (1974).
11. D. L. Jeanmaire and R. P. V. Duyne, "Surface Raman spectroelectrochemistry: Part I. Heterocyclic, aromatic, and aliphatic amines adsorbed on the anodized silver electrode," J. Electroanal. Chem. **84**, 1–20 (1977).
12. M. Moskovits, "Surface-enhanced spectroscopy," Rev. Mod. Phys. **57**, 783–826 (1985).
13. W. L. Barnes, A. Dereux, and T. W. Ebbesen, "Surface plasmon subwavelength optics," Nature **424**, 824–830 (2003).
14. J. R. Lakowicz, C. D. Geddes, I. Gryczynski, J. Malicka, Z. Gryczynski, K. Aslan, J. Lukomska, E. Matveeva, J. Zhang, R. Badugu, and J. Huang, "Advances in surface-enhanced fluorescence," J. Fluoresc. **14**, 425–441 (2004).
15. E. Fort and S. Grésillon, "Surface enhanced fluorescence," J. Phys. D **41**, 013001 (2008).
16. H. Chew, D. S. Wang, and M. Kerker, "Surface enhancement of coherent anti-Stokes Raman scattering by colloidal spheres," J. Opt. Soc. Am. B **1**, 56–66 (1984).
17. T. Ichimura, N. Hayazawa, M. Hashimoto, Y. Inouye, and S. Kawata, "Local enhancement of coherent anti-Stokes Raman scattering by isolated gold nanoparticles," J. Raman Spectrosc. **34**, 651–654 (2003).
18. T. W. Koo, S. Chan, and A. A. Berlin, "Single-molecule detection of biomolecules by surface-enhanced coherent anti-Stokes Raman scattering," Opt. Lett. **30**, 1024–1026 (2005).
19. V. Namboodiri, M. Namboodiri, G. I. Cava-Diaz, M. Oppermann, G. Flachenecker, and A. Materny, "Surface-enhanced femtosecond CARS spectroscopy (SE-CARS) on pyridine," Vib. Spectrosc. **56**, 9–12 (2011).
20. C. Steuwe, C. F. Kaminski, J. J. Baumberg, and S. Mahajan, "Surface enhanced coherent anti-Stokes Raman scattering on nanostructured gold surfaces," Nano Lett. **11**, 5339–5343 (2011).
21. R. R. Frontiera, A. I. Henry, N. L. Gruenke, and R. P. Van Duyne, "Surface-enhanced femtosecond stimulated Raman spectroscopy," J. Phys. Chem. Lett. **2**, 1199–1203 (2011).
22. S. Palomba and L. Novotny, "Nonlinear excitation of surface plasmon polariton by four-wave mixing," Phys. Rev. Lett. **101**, 056802 (2008).
23. J. Renger, R. Quidant, N. V. Hulst, S. Palomba, and L. Novotny, "Free-space excitation of propagating surface plasmon polaritons by nonlinear four-wave-mixing," Phys. Rev. Lett. **103**, 266802 (2009).
24. J. Renger, R. Quidant, N. V. Hulst, and L. Novotny, "Surface-enhanced nonlinear four-wave-mixing," Phys. Rev. Lett. **104**, 046803 (2010).
25. S. Palomba, S. Zhang, Y. Park, G. Bratal, X. Yin, and X. Zhang, "Optical negative refraction by four-wave mixing in thin metallic nanostructures," Nat. Mater. **11**, 34–38 (2012).
26. C. K. Chen, A. R. B. de Castro, and Y. R. Shen, "Surface coherent anti-Stokes Raman spectroscopy," Phys. Rev. Lett. **43**, 946–949 (1979).
27. X. Liu, Y. Wang, and E. O. Potma, "Surface-mediated four-wave mixing of nanostructures with counterpropagating surface plasmon polaritons," Opt. Lett. **36**, 2348–2350 (2011).
28. D. Axelrod, T. P. Burghardt, and N. L. Thompson, "Total internal reflection fluorescence," Annu. Rev. Biophys. Bioeng. **13**, 247–268 (1984).
29. J. D. Jackson, *Classical Electrodynamics* (Wiley, 1975).
30. T. Funantsu, Y. Harada, M. Tokunaga, K. Saito, and T. Yanagida, "Imaging of single fluorescent molecules and individual ATP turnovers by single myosin molecules in aqueous solution," Nature **374**, 555–559 (1995).
31. R. Y. He, G. L. Chang, H. L. Wu, C. H. Lin, K. C. Chiu, Y. D. Su, and S. J. Chen, "Enhanced live cell membrane imaging using surface plasmon-enhanced total internal reflection fluorescence microscopy," Opt. Express **14**, 9307–9316 (2006).
32. R. Y. He, Y. D. Su, K. C. Cho, C. Y. Lin, N. S. Chang, C. H. Chang, and S. J. Chen, "Surface plasmon-enhanced two-photon fluorescence microscopy for live cell membrane imaging," Opt. Express **17**, 5987–5997 (2009).
33. R. M. Corn, M. Romagnoli, M. D. Levenson, and M. R. Philpott, "Second harmonic generation at thin film silver electrodes via surface polaritons," J. Chem. Phys. **81**, 4127–4132 (1984).
34. C. Qian, T. S. Velinov, M. C. Pitter, and M. G. Somekh, "Surface plasmon-assisted widefield non-linear imaging of gold structures," J. Microsc. **229**, 6–11 (2008).
35. C. Heinrich, S. Bernet, and M. Ritsch-Marte, "Wide-field coherent anti-Stokes Raman scattering microscopy," Appl. Phys. Lett. **84**, 816–818 (2004).
36. I. Toytman, K. Cohn, T. Smith, D. Simanovskii, and D. Palanker, "Wide-field coherent anti-Stokes Raman scattering microscopy with non-phase-matching illumination," Opt. Lett. **32**, 1941–1943 (2007).
37. A. Jesacher, C. Roider, S. Khan, G. Thalhammer, S. Bernet, and M. Ritsch-Marte, "Contrast enhancement in widefield CARS microscopy by tailored phase-matching using a spatial light modulator," Opt. Lett. **36**, 2245–2247 (2011).
38. J. X. Cheng, A. Volkmer, and X. S. Xie, "Theoretical and experimental characterization of coherent anti-Stokes Raman scattering microscopy," J. Opt. Soc. Am. B **19**, 1363–1375 (2002).
39. E. O. Potma and X. S. Xie, "Detection of single lipid bilayers with coherent anti-Stokes Raman scattering (CARS) microscopy," J. Raman Spectrosc. **34**, 642–650 (2003).
40. J. Renger, R. Quidant, and L. Novotny, "Enhanced nonlinear response from metal surfaces," Opt. Express **19**, 1777–1785 (2011).